Reverse-time migration using the energy imaging condition in isotropic and VTI media

Alejandro Cabrales-Vargas

ABSTRACT

The recently proposed concept of energy imaging condition is an alternative method for the attenuation of low-wavenumber artifacts that arise in reverse-time migration. It can be set in terms of energy conservation of the wave equation solution, or using the impedance kernel, and can be implemented in acoustic and elastic media. I introduce an implementation of the energy imaging condition in vertical transverse isotropic media. The performance of the energy imaging condition is evaluated in 2-D synthetic data, both isotropic and anisotropic.

INTRODUCTION

Reverse-time migration (RTM) (Baysal et al., 1983; Kosloff and Baysal, 1983; Gazdag and Carrizo, 1986; McMechan, 1983) is the best available solution in oil & gas exploration to image the complexity of the subsurface. The capability of two-way wave propagation to represent complex wavepaths makes possible to image complex structures, formerly addressed (often imperfectly) by distinct versions of one-way wave propagation (e.g. Stoffa et al., 1990; Ristow and Rühl, 1994; Biondi, 2002). Notwithstanding their level of sophistication, one-way wave equation methods cannot use prismatic trajectories to image important oil and gas reservoirs, such as sandstones terminations against salt flanks beneath salt canopies. RTM resolves such complexities because it accounts for upgoing and downgoing trajectories, turning waves, and headwaves. The current practice is constructing the image using zero-lag time crosscorrelation (Claerbout, 1971) of the source wavefield and the receiver wavefield.

However, RTM suffers from low-wavenumber artifacts, unique in this technique. The crosscorrelation imaging condition does not distinguish the source and receiver wavefields interacting at the seismic reflections (traveling at opposite directions), from the case when they travel in the same direction and interact along the way, producing such artifacts.

There has been extensive research devoted to attenuating the RTM low-wavenumber artifacts while preserving the quality of the image. One of the simplest solutions consists of smoothing the velocity field. However, some images require preserving sharp velocity contrasts to maintain accuracy, such as the case of models containing salt-sediment interfaces. Yoon and Marfurt (2006) proposed filtering propagation angles

by computing Poynting vectors, which requires accurate computations of the time derivatives of the wavefields. Liu et al. (2011) proposed wavefield separation in the Fourier domain, thereby enforcing correlations of wavefield components propagating in opposite directions. Despite its effectiveness, this technique requires four 1-D Fourier transforms along the z axis per time step (one forward-inverse transform pair per wavefield), hence considerably increases the computational time.

A recent solution consists of an imaging condition based on the concept of the impedance kernel. This idea is borrowed from the full-waveform inversion optimization problem (Tarantola, 1984), usually formulated under the concept of the adjoint-state method (Fichtner, 2011; Plessix, 2006). Zhu et al. (2011) employ such idea for elastic and time-lapse imaging conditions, whereas Pestana and dos Santos (2014) proposed an implementation in conjunction with the Poynting vector. Meanwhile, based on the theory of seismic inverse scattering, Whitmore and Crawley (2012) proposed virtually the same solution using approximations of the source and receiver ray parameters. The result is two images: one based on the wavefields time derivatives, and other based on the spatial gradients. Adding the images cancels almost entirely the low-wavenumber artifacts while retaining the reflectivity. More recently, Rocha et al. (2015a) arrived to the same method with the principle of conservation of the energy of the acoustic wave equation. This solution makes use of the energy as a norm to define an inner-product in space-time. Components of the source wavefield and the receiver wavefield become orthogonal under such inner-product. Choosing these components to be backscattering and turning waves, one attenuates the low-wavenumber artifacts. The idea is extended to the elastic case by Rocha et al. (2015b).

This report is organized as follows. I first make a review of the energy imaging condition. Next, I introduce an energy imaging condition for VTI media. Next, I show the results obtained for isotropic and VTI synthetic datasets. Finally, I present the conclusions of this work.

ENERGY IMAGING CONDITIONS

Imaging in space-time or the adjoint-state method

Rocha et al. (2015a) prove that from the principle of conservation of energy of the acoustic wave equation, if $u(\mathbf{x}, t)$ represents solution of such wave equation, then the energy as function of time is given by

$$E(t) = \int_{\Omega} \left[\frac{1}{v^2} \left(\frac{\partial u}{\partial t} \right)^2 + \|\nabla u\|^2 \right] d\mathbf{x}, \tag{1}$$

which can be regarded as a norm. Shifting the integration to the time domain, the following inner-product can be derived for any two solutions $u_1(\mathbf{x}, t)$ and $u_2(\mathbf{x}, t)$:

$$\sum_t \left[(\cos 2\theta_c) \frac{1}{v} \frac{\partial u_1}{\partial t} \frac{1}{v} \frac{\partial u_2}{\partial t} + \nabla u_1 \cdot \nabla u_2 \right], \tag{2}$$

where $v(\mathbf{x})$ is the acoustic velocity, and $2\theta_c$ is a cut-off angle between the u_1 and u_2 wavepaths at any position.

Equation 1 constitutes an inner-product of vectors defined as $(\frac{1}{v(\mathbf{x})}\frac{\partial u}{\partial t}, \nabla u)$: a gradient in space-time. Selected components become orthogonal for an imposed reflection cut-off angle, $\cos(2\theta_c)$. Now we can substitute the source wavefield, $S(\mathbf{x}, t)$, and the receiver wavefield, $R(\mathbf{x}, t)$, in Equation2. Setting $\theta_c = 0$, we obtain the following inner-product (Rocha et al., 2015a),

$$I(\mathbf{x}) = \sum_t \Box S(\mathbf{x}, t) \cdot \Box R(\mathbf{x}, t), \tag{3}$$

where $I(\mathbf{x})$ represents a migrated image, and the operator $\Box$ constitutes the gradient operator in space-time:

$$\Box = \left(\frac{1}{v(\mathbf{x})}\frac{\partial}{\partial t}, \nabla\right). \tag{4}$$

Equation 3 represents the *energy imaging condition* for $\theta_c = 0$. It enhances the tomographic component of the image, i.e., the low-wavenumber artifacts related to backscattering and diving waves. To attenuate such tomographic component we set $\theta = 90°$, so the energy imaging condition becomes

$$I(\mathbf{x}) = \sum_t \Box S(\mathbf{x}, t) \cdot \widetilde{\Box} R(\mathbf{x}, t), \tag{5}$$

where $\widetilde{\Box}$ is defined as

$$\widetilde{\Box} = \left(-\frac{1}{v(\mathbf{x})}\frac{\partial}{\partial t}, \nabla\right). \tag{6}$$

Equation 5 is explicitly represented as

$$I(\mathbf{x}) = \sum_t \left[-\frac{1}{v(\mathbf{x})^2}\frac{\partial S(\mathbf{x}, t)}{\partial t}\frac{\partial R(\mathbf{x}, t)}{\partial t} + \nabla S(\mathbf{x}, t) \cdot \nabla R(\mathbf{x}, t)\right]. \tag{7}$$

The negative sign in Equation 7 corresponds to the cosine term evaluated at $2\theta = 180°$, *i.e.*, when the wavepaths travel in the same direction (Whitmore and Crawley, 2012). The energy imaging condition vanishes at such angle, so the low-wavenumber artifacts are attenuated and the seismic reflections are preserved.

It is interesting to notice that Equation 7 can be obtained using the adjoint-state method (Tarantola, 1984; Plessix, 2006). Setting the density and the P-wave velocity as independent parameters (Fichtner, 2011) we can obtain the *impedance kernel*, K_I, as a linear combination of the density kernel, K_ρ, and the bulk density kernel, K_K, (after dropping the shear velocity terms) as follows (Fichtner, 2011)

$$K_I = K_\rho + v^2 K_K, \tag{8}$$

where $v = \sqrt{\frac{K}{\rho}}$ is the P-wave propagation velocity,

$$K_\rho = -\int_t \frac{\partial \lambda}{\partial t}\frac{\partial u}{\partial t} dt, \tag{9}$$

and

$$K_K = \int_t \nabla\lambda \cdot \nabla u dt. \tag{10}$$

so the impedance sensitivity kernel becomes

$$K_I = \int_t \Big[- \frac{\partial \lambda}{\partial t} \frac{\partial u}{\partial t} + v^2 \nabla\lambda \cdot \nabla u \Big] dt. \tag{11}$$

u represents the synthetic wavefield obtained by forward propagating a discrete source function with the acoustic wave equation, for any choice of model parameters. λ represents the wavefield obtained by backward propagating the data residual (difference between synthetic data and recorded data) with the acoustic wave equation, using the same choice of model parameters. Equations 9 and 10 are obtained applying the adjoint-state method to the full waveform inversion (FWI) optimization problem (Tarantola, 1984; Tromp et al., 2005; Fichtner, 2011).

Now we substitute in Equation 11 the source wavefield, S, and the receiver wavefield, R, obtaining

$$I(\mathbf{x}) = \int_t \Big[- \frac{\partial S}{\partial t} \frac{\partial R}{\partial t} + v^2 \nabla S \cdot \nabla R \Big] dt, \tag{12}$$

which is equivalent to Equation 7.

The energy imaging condition requires space and time derivatives of the source wavefield and the receiver wavefield. The space derivatives can be computed using staggered grids, which can be efficiently implemented with parallel computational schemes. The time derivatives can be implemented at almost not additional cost using a simple procedure described in the **Appendix**.

Energy imaging condition for vertical transverse isotropy

In this section I derive an energy imaging condition in acoustic vertical transversely isotropic (VTI) medium. I begin with the VTI wave equations proposed by Zhang et al. (2011) (their equation 15) in 2-D:

$$\frac{1}{v^2} \frac{\partial^2 \mathbf{p}}{\partial t^2} = \mathbf{B}\mathbf{D}\mathbf{p}, \tag{13}$$

where $\mathbf{p} = [p \quad r]^T$ is the stress vector, p and r are the horizontal and vertical stress components, respectively, matrices $\mathbf{B}$ and $\mathbf{D}$ are defined as

$$\mathbf{B} = \begin{bmatrix} 1+2\epsilon & \sqrt{1+2\delta} \\ \sqrt{1+2\delta} & 1 \end{bmatrix}$$

and

$$\mathbf{D} = \begin{bmatrix} \dfrac{\partial^2}{\partial x^2} & 0 \\ 0 & \dfrac{\partial^2}{\partial z^2} \end{bmatrix},$$

and ϵ and δ are the Thomsen anisotropy parameters (Thomsen, 1986).

Zhang et al. (2011) derive an expression to quantify the energy of their tilted-transversely isotropic (TTI) RTM equation, which I apply to the 2-D VTI version (Equation 13),

$$E(t) = \int_\Omega \left\{ \frac{1}{v^2} [\mathbf{Y}\dot{\mathbf{p}}]^T \mathbf{\Lambda}^{-1} \mathbf{Y}\dot{\mathbf{p}} + \left(\frac{\partial p}{\partial x}\right)^2 + \left(\frac{\partial r}{\partial z}\right)^2 \right\} d\mathbf{x}, \tag{14}$$

where $\dot{\mathbf{p}}$ is the time derivative of vector $\mathbf{p}$, and matrices $\mathbf{Y}$ and $\mathbf{\Lambda}$ are obtained from the diagonalization of matrix $\mathbf{B}$,

$$\mathbf{B} = \mathbf{Y}^T \mathbf{\Lambda} \mathbf{Y},$$

and are given by (Zhang et al., 2011)

$$\mathbf{Y} = \frac{1}{d} \begin{bmatrix} a & b \\ -b & a \end{bmatrix},$$

and

$$\mathbf{\Lambda} = \begin{bmatrix} \lambda_+ & 0 \\ 0 & \lambda_- \end{bmatrix},$$

and where $\lambda_\pm = 1 + \epsilon \pm \sqrt{(1+\epsilon)^2 - 2(\epsilon - \delta)}$ are the eigenvalues of matrix $\mathbf{B}$, $a = \epsilon + \sqrt{(1+\epsilon)^2 - 2(\epsilon - \delta)}$, $b = \sqrt{1 + 2\delta}$, and $d = \sqrt{a^2 + b^2}$.

Zhang et al. (2011) use Equation 14 to prove the stability of their TTI RTM equation. I use this expression as an energy norm (Rocha et al., 2015a,b) to derive the energy imaging condition for VTI RTM.

Let $\mathbf{p}_S = [p_S \quad r_S]^T$ and $\mathbf{p}_R = [p_R \quad r_R]^T$ be the stress vectors corresponding to the source wavefield and the receiver wavefield, respectively. We substitute them in Equation 14, and integrate in time rather than in space:

$$I(\mathbf{x}) = \int_t \Box \mathbf{p}_S \cdot \Box \mathbf{p}_R dt = \int_t \left\{ \frac{1}{v^2} [\mathbf{Y}\dot{\mathbf{p}}_S]^T \mathbf{\Lambda}^{-1} \mathbf{Y}\dot{\mathbf{p}}_R + \left(\frac{\partial p_S}{\partial x}\right)\left(\frac{\partial p_R}{\partial x}\right) + \left(\frac{\partial r_S}{\partial z}\right)\left(\frac{\partial r_R}{\partial z}\right) \right\} dt. \tag{15}$$

This expression corresponds to the cut-off angle $\theta_{cut} = 0°$. It attenuates the reflections and exacerbates the tomographic component. Using a similar definition of $\tilde{\Box}$ as in Equation 6, we obtain

$$I(\mathbf{x}) = \int_t \Box \mathbf{p}_S \cdot \tilde{\Box} \mathbf{p}_R dt = \int_t \left\{ \frac{1}{v^2} [\mathbf{Y}\dot{\mathbf{p}}_S]^T \mathbf{\Lambda}^{-1} \mathbf{Y}\dot{\mathbf{p}}_R - \left(\frac{\partial p_S}{\partial x}\right)\left(\frac{\partial p_R}{\partial x}\right) - \left(\frac{\partial r_S}{\partial z}\right)\left(\frac{\partial r_R}{\partial z}\right) \right\} dt. \tag{16}$$

Equation 16 corresponds to the cut-off angle $\theta_{cut} = 90°$, thereby the image will preserve the reflections and attenuate the low-wavenumber artifacts. An small inconvenient occurs in zero-anisotropy areas because λ_- is zero and matrix Λ becomes singular. On can prevent such singularity by adding a tiny positive value.

Normalizing the image

RTM imaging conditions often require normalization to balance the amplitudes. Normalizations have been proposed respect to either the sources or the receivers; shot-by-shot, global, or hybrid normalizations (Cogan et al., 2011). I use a shot-by-shot normalization scheme.

For conventional crosscorrelation imaging condition, the normalized image can be obtained as

$$I_N(\mathbf{x}) = \sum_{shots} \frac{\sum_t S(\mathbf{x},t)R(\mathbf{x},t)}{\left\{\sum_t S(\mathbf{x},t)S(\mathbf{x},t)\right\}}, \tag{17}$$

and for the energy imaging condition,

$$I_N(\mathbf{x}) = \sum_{shots} \frac{\sum_t \Box S(\mathbf{x},t)\cdot \Box R(\mathbf{x},t)}{\left\{\sum_t \Box S(\mathbf{x},t)\cdot \Box S(\mathbf{x},t)\right\}}. \tag{18}$$

The symbol $\{\}$ signifies the application of smoothing imaging condition (Guitton et al., 2007). This avoids divisions by zero by smearing the energy, with the application of a triangle filter.

NUMERICAL EXAMPLES

In this section I compare RTM images using the crosscorrelation imaging condition (CIC) with the energy imaging condition (EIC). The experiments are performed on one isotropic model (SEG/EAGE salt model) and two anisotropic models (Marmousi VTI model and Hess VTI salt model). I slightly smoothed the model parameters (velocity and anisotropy) so the image keeps accuracy and produces low-wavenumber artifacts.

The RTM code used in the computations is based on a finite differences solution of the two-way wave equation, implemented with the Lax-Wendroff method. I use random boundary conditions (Clapp, 2009, 2010) to reduce the computational memory burden. Mild numerical artifacts derived from such boundary conditions can be observed in the images.

2-D SEG/EAGE salt model

This isotropic model is a vertical slice of the original 3-D SEG/EAGE model, which was extracted by O'Brien and Gray (1996).

Figure 1 shows the RTM image using CIC. Despite the velocity smoothing, low-wavenumber artifacts still manifest. Further smoothing would progressively attenuate such artifacts, but at the cost of accuracy loss in reflections positioning and focusing.

Figure 2 shows the RTM image using EIC with $\theta_c = 0°$. The reflections have been attenuated and the tomographic component of the image is preserved. The reason for the persistance of some reflections is because they are not confined to the narrow rejection band around normal incidence.

Figure 3 shows the RTM image using EIC with $\theta_c = 90°$. This time the low-wavenumber artifacts have been virtually eliminated from the image, and many features formerly obscured become evident. Note, however, that the two steep normal faults on top of the salt body ($x \approx 20000$ ft and $x \approx 25000$ m) lose definition, while they clearly manifest in Figure 2. One explaination is that steep events are better imaged by wide reflection angles, especially at shallow depths. The energy of such wide angles is likely to be partially attenuated. A modified version of EIC would be needed to preserve such important features, and it is a subject for future research.

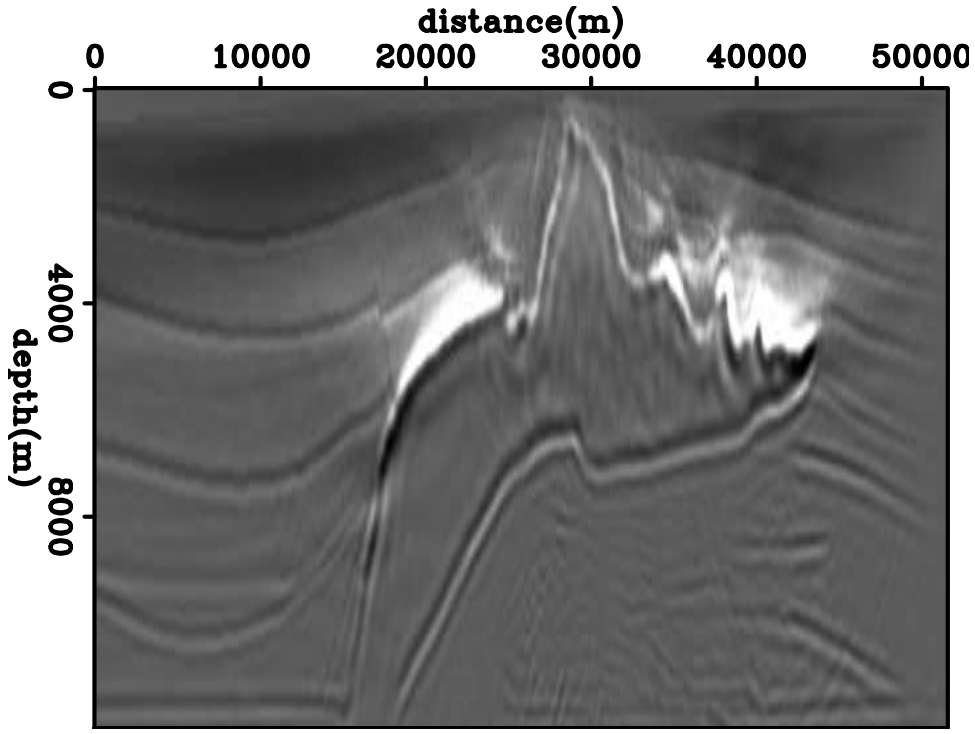

Figure 1: 2-D SEG/EAGE salt model after RTM using the correlation imaging condition [**CR**].

Marmousi VTI model

This anisotropic model was created by Tariq Alkhalifah (Alkhalifah, 1997). It has only one anisotropic parameter, η, that constitutes the entry for ϵ, whereas δ is set to zero (Alkhalifah, personal communication).

Figure 4 shows the RTM image using CIC. The anisotropic solution performs well, imaging the reflections to their correct positions. This constitutes a stable finite-

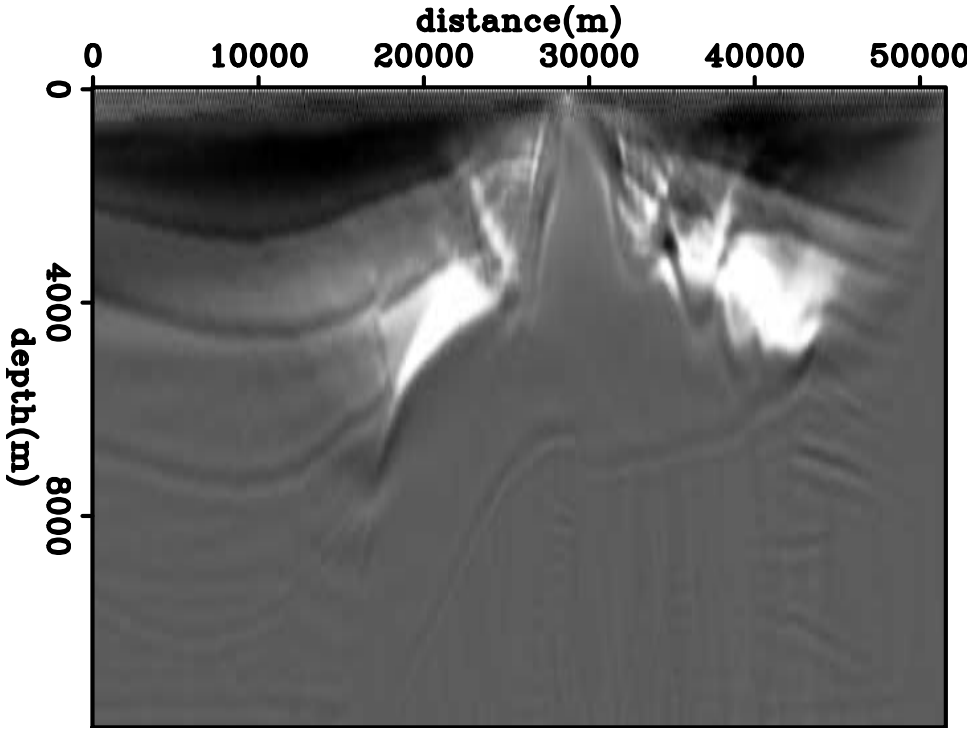

Figure 2: 2-D SEG/EAGE salt model after RTM using the energy imaging condition for $\theta = 0°$ [**CR**].

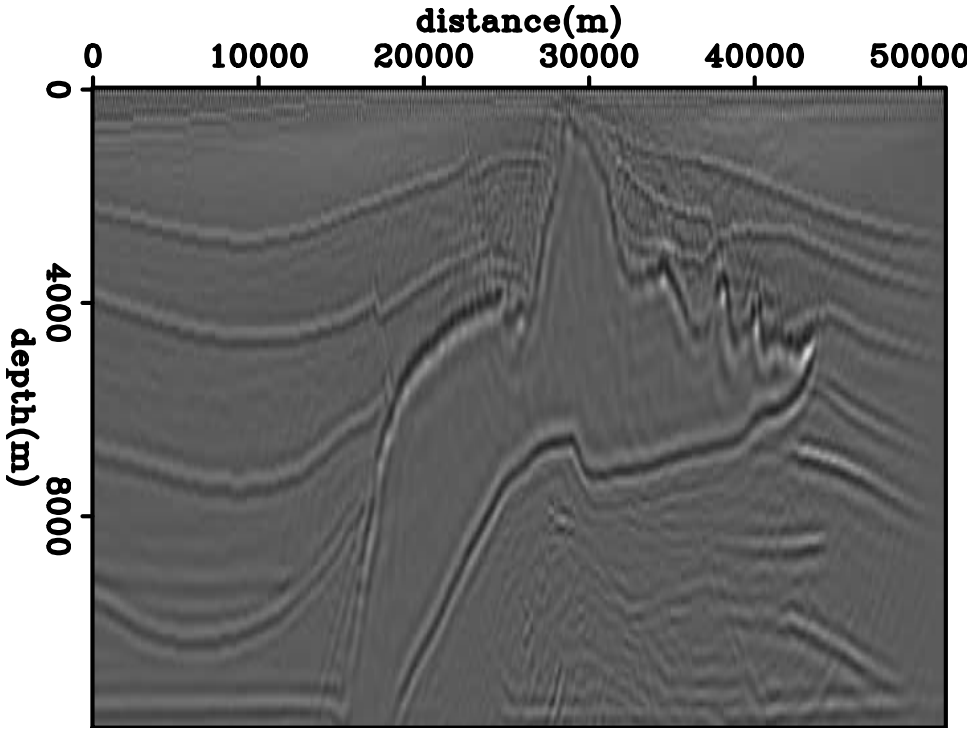

Figure 3: 2-D SEG/EAGE salt model after RTM using the energy imaging condition for $\theta = 90°$ [**CR**].

difference solution, as far as $\epsilon \geqslant \delta$ (Zhang et al., 2011). Similarly to the previous example, the low-wavenumber artifacts could not be prevented by slightly smoothing the velocity model.

Figure 5 shows the RTM image using EIC with $\theta_c = 0°$. In contrast to the previous example (Figure 2), we observe comparatively less reflections "leaking" into the image, so the tomographic component prevails, as expected. This image corresponds to the application of Equation 15 plus normalization (Equation 18).

Figure 6 shows the RTM image using EIC with $\theta_c = 90°$. Most of the low-wavenumber artifacts are attenuated. This result and the previous one prove that the proposed VTI energy imaging condition (Equations 15 and 16) works as expected. Moreover, in this case the steep dipping events (fault planes and fold limbs) are well preserved.

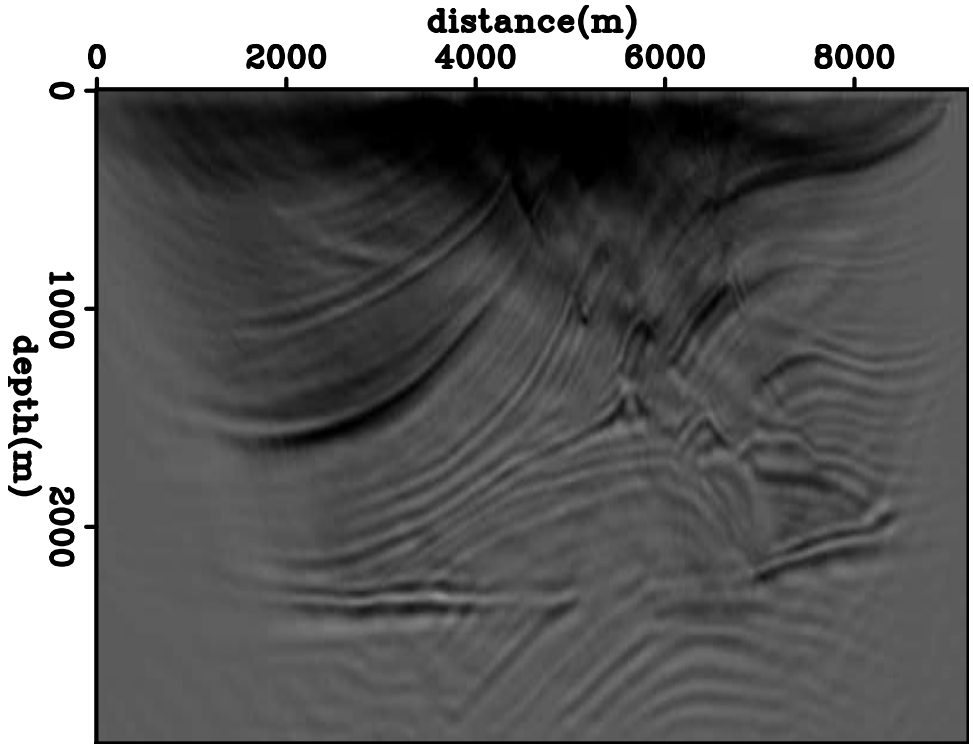

Figure 4: Marmousi VTI model after RTM using the correlation imaging condition [**CR**].

Hess VTI salt model

The Hess VTI model was created by Hess Corporation. There are two versions of the synthetic data. I use the version without surface multiples, created with the SEP libraries. This model has non-zero ϵ and δ model parameters.

Figure 7 shows the RTM image using CIC. In this case, slightly smoothing the

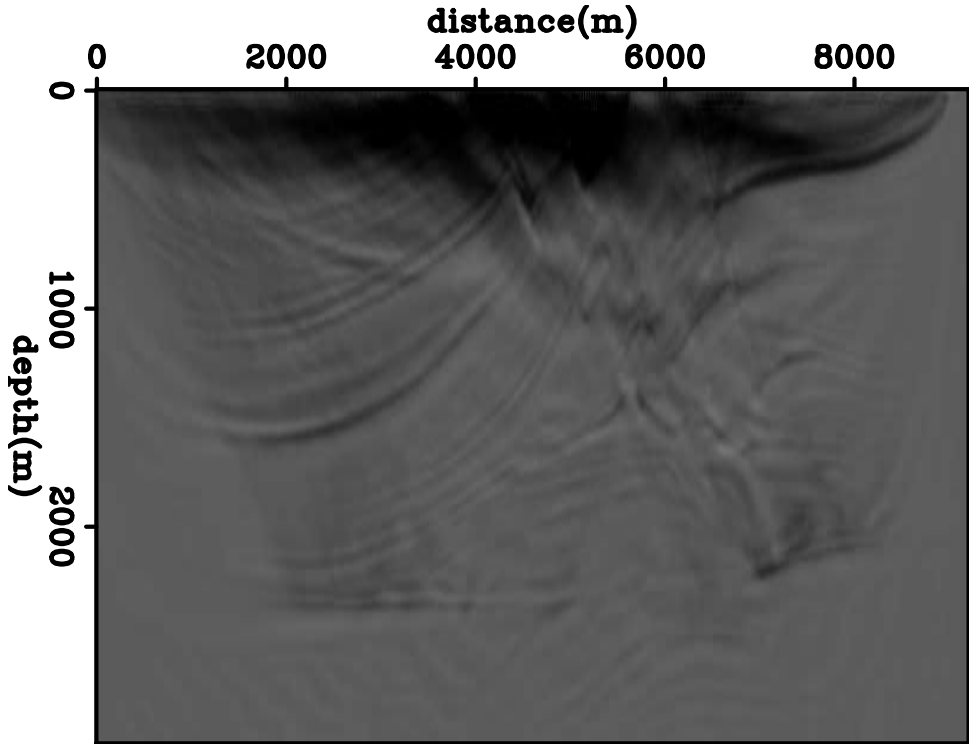

Figure 5: Marmousi VTI model after RTM using the energy imaging condition for $\theta = 0°$ [**CR**].

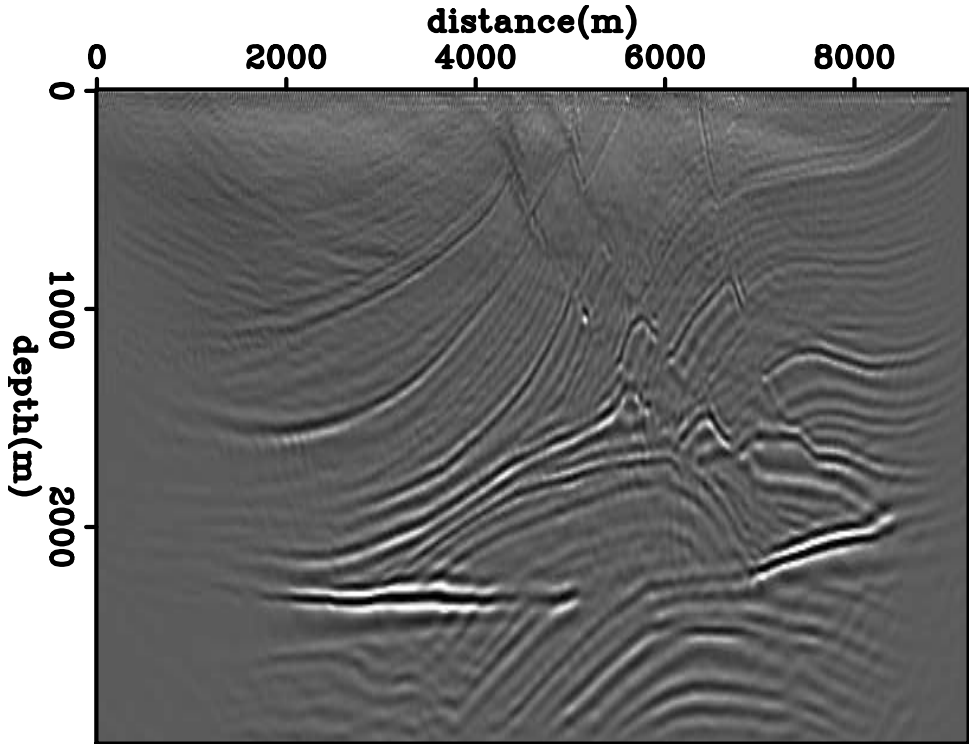

Figure 6: Marmousi VTI model after RTM using the energy imaging condition for $\theta = 90°$ [**CR**].

model parameters reduced some of the low-wavenumber artifacts, except at the salt reflection and in the shallow part, where some backscattering is expected as consequence of the long offset (26000 ft). Low-wavenumber streaks vertically cross deep sediments and the salt body, around $x = 20000$ ft. The random boundary implementation does not address such low-wavenumber propagations (Shen and Clapp, 2011).

Figure 8 shows the RTM image using EIC with $\theta_c = 0°$. Almost all deep reflections are rejected. Only low-wavenumber components of shallower reflections are imaged. The low-wavenumber streaks become clearer.

Figure 9 shows the RTM image using EIC with $\theta_c = 90°$. In this case some low-wavenumber artifacts leak, but the image is quite acceptable. Faults and other steep dipping events are well preserved. The low-wavenumber streaks are virtually eliminated.

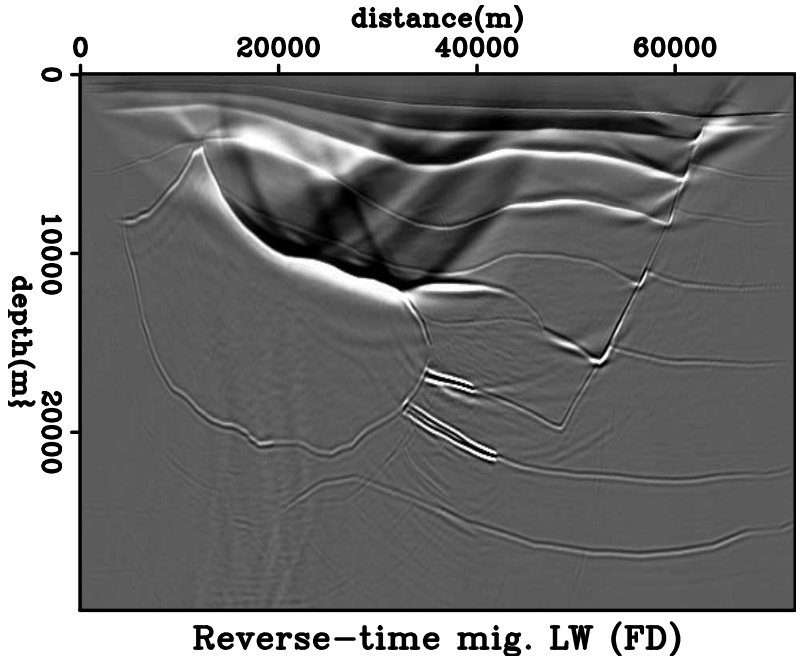

Figure 7: Hess salt VTI model after RTM using the correlation imaging condition [**CR**].

CONCLUSIONS

The energy imaging condition constitutes a viable alternative for attenuating RTM low-wavenumber artifacts. It is derived from the principle of conservation of energy of the wave equation. It too can be derived from the impedance kernel concept, using the adjoint-state method. The principle behind the energy imaging condition is to selectively make components of the source wavefield and the receiver wavefield

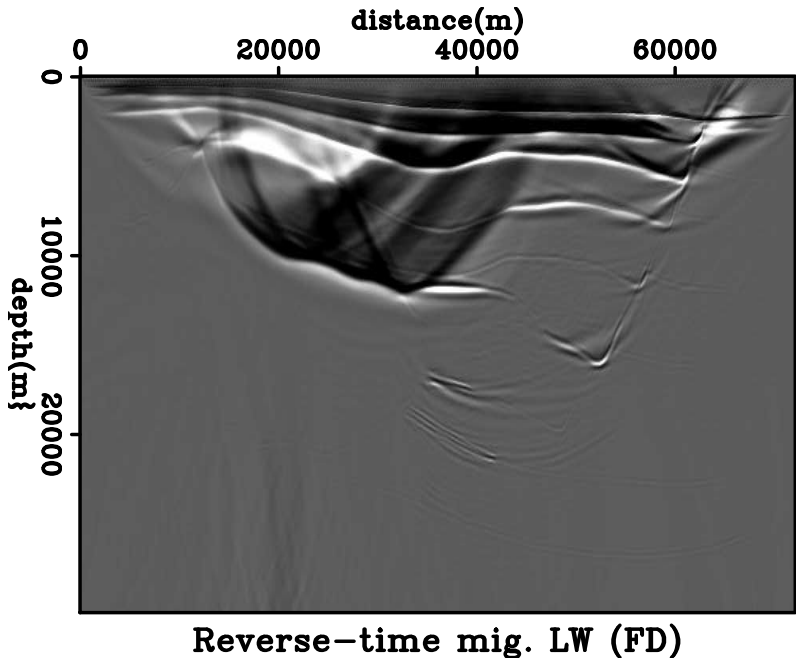

Figure 8: Hess salt VTI model after RTM using the energy imaging condition for $\theta = 0^\circ$ [**CR**].

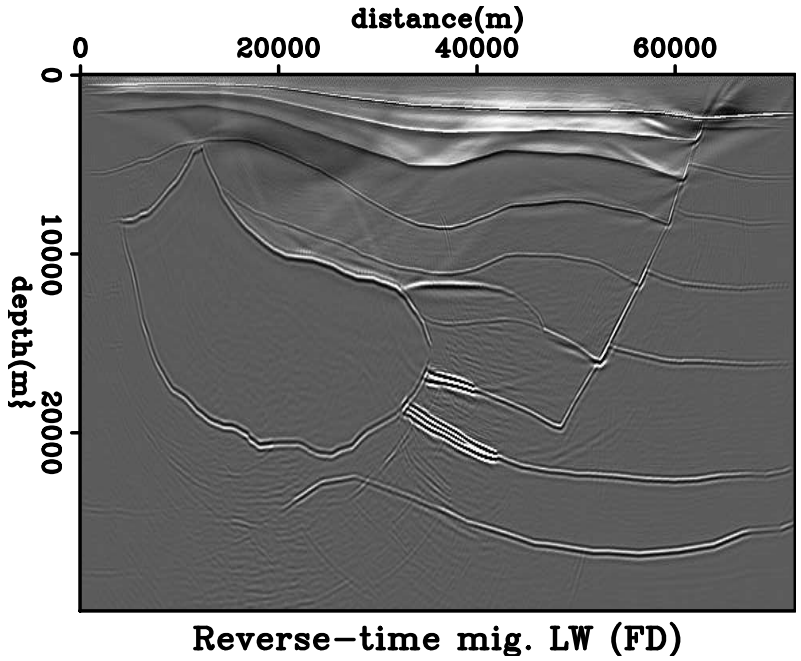

Figure 9: Hess salt VTI model after RTM using the energy imaging condition for $\theta = 90^\circ$ [**CR**].

mutually orthogonal in space-time. The key is to make orthogonal the wavefield components that we do not want to image, such as backscattering and direct waves.

I introduced an energy imaging condition for VTI media based on the principle of conservation of energy (Zhang et al., 2011). It can potentially be expanded to TTI.

The numerical examples showed that the energy imaging condition generally attenuates the low-wavenumber artifacts in a satisfactory manner. However, the application in the 2-D SEG/EAGE salt model exhibited slight removal of useful signal. In the anisotropic models the proposed solution worked well, although it left some weak artifacts in the Hess VTI salt model. According to these results, future research is needed to better tune the final image. The potential use of EIC is not limited to obtaining cleaner RTM images, but it can be employed to isolate the tomographic component (Rocha et al., 2015a) for the computation of the FWI gradient.

ACKNOWLEDGMENTS

I would like to thank Biondo Biondi for the conversation that motivated me to prepare this report. Thanks to Tariq Alkhalifah for his anisotropic version of the Marmousi model, and to Hess Corporation for their salt VTI model. Thanks to the SEP sponsors for their continuous support. Special thanks to Huy Le and Yinbin Ma, for their thorough review and the useful discussions. Finally, and no less important, thanks to Petróleos Mexicanos for their financial support.

REFERENCES

Alkhalifah, T., 1997, An anisotropic Marmousi model: SEP-Report, **95**, 265–282.

Baysal, E., D. Kosloff, and J. Sherwood, 1983, Reverse time migration: Geophysics, **48**, 1514–1524.

Biondi, B., 2002, Stable wide-angle Fourier finite-difference downward extrapolation of 3-D wavefields: Geophysics, **67**, 872–882.

Claerbout, J., 1971, Toward a unified theory of reflector mapping: Geophysics, **36**, 467–481.

Clapp, R. G., 2009, Reverse time migration with random boundaries: SEP-Report, **138**, 29–38.

———, 2010, More fun with random boundaries: SEP-Report, **140**, 95–102.

Cogan, M., R. Fletcher, R. King, and D. Nichols, 2011, Normalization strategies for reverse-time migration: SEG Technical Program Expanded Abstracts 2011, 3275–3279.

Fichtner, A., 2011, Full seismic waveform modelling and inversion: Springer Science & Business Media.

Gazdag, J. and E. Carrizo, 1986, On reverse-time migration: Geophysical Prospecting, **34**, 822–832.

Guitton, A., A. Valenciano, D. Bevc, and J. Claerbout, 2007, Smooting imaging condition for shot-profile migration: Geophysics, **72**, no. 3, S149–S154.

Kosloff, D. and E. Baysal, 1983, Migration with the full acoustic wave equation: Geophysics, **48**, 677–687.

Liu, F., Z. Guanquan, S. Morton, and J. Leveille, 2011, An effective imaging condition for reverse-time migration using wavefield decomposition: Geophysics, **76**, no. 1, S29–S39.

McMechan, G., 1983, Migration by extrapolation of time-dependent boundary values: Geophysical Prospecting, **31**, 413–420.

O'Brien, M. and S. Gray, 1996, Can we image beneath salt?: The Leading Edge, **15**, no. 1, 17–22.

Pestana, R. and A. dos Santos, 2014, RTM imaging condition using impedance sensitivity kernel combined with Poynting vector: SEG Technical Program Expanded Abstracts 2014, 3763–3768.

Plessix, R., 2006, A review of the adjoint-state method for computing the gradient of a functional with geophysical applications: Geophysical Journal International, **167**, 495–503.

Ristow, D. and T. Rühl, 1994, Fourier finite-difference migration: Geophysics, **59**, 1882–1893.

Rocha, D., N. Tanushev, and P. Sava, 2015a, Acoustic wavefield imaging using the energy norm: SEG Technical Program Expanded Abstracts 2015, 4085–4090.

———, 2015b, Elastic wavefield imaging using the energy norm: SEG Technical Program Expanded Abstracts 2015, 2124–2128.

Shen, X. and R. G. Clapp, 2011, Random boundary condition for low-frequency wave propagation: SEP-Report, **143**, 85–92.

Stoffa, P., J. Fokkema, de Luna Freire R., and W. Kessinger, 1990, Split-step Fourier migration: Geophysics, **56**, 410–421.

Tarantola, A., 1984, Inversion of seismic reflection data in the acoustic approximation: Geophysics, **49**, 1259–1266.

Thomsen, L., 1986, Weak elastic anisotropy: Geophysics, **51**, 1954–1996.

Tromp, J., C. Tape, and Q. Liu, 2005, Seismic tomography, adjoint methods, time reversal and banana-doughnut kernels: Geophysical Journal International, **160**, 195–216.

Whitmore, N. and S. Crawley, 2012, Applications of RTM inverse scattering imaging conditions: SEG Technical Program Expanded Abstracts 2012, 1–6.

Yoon, K. and K. Marfurt, 2006, Reverse-time migration using the Poynting vector: Exploration Geophysics, **37**, 102–107.

Zhang, Y., H. Zhang, and G. Zhang, 2011, A stable TTI reverse time migration and its implementation: Geophysics, **76**, no. 3, WA3–WA11.

Zhu, H., Y. Luo, T. Nissen-Meyer, C. Morency, and J. Tromp, 2011, Elastic imaging and time-lapse migration based on adjoint methods: Geophysics, **74**, no. 6, WCA167–WCA177.

APPENDIX

The energy imaging condition requires time derivatives of the source wavefied and the receiver wavefield. It is inefficient (and very likely inaccurate) to obtain the derivatives numerically out of a number of time frames stored in memory, worse yet as an independent computation. A better idea is computing the first derivatives by "recycling" terms employed to compute the plain wavefields. In the following derivation I omit the space dependencies for the sake of simplicity.

Let $u(t \pm \Delta t)$ represent both the wavefield forward stepped in time (positive sign) and the wavefield backward stepped in time (negative sign). We can expand it in Taylor series around $u(t)$:

$$u(t \pm \Delta t) = u(t) \pm \Delta t \frac{\partial u(t)}{\partial t} + \frac{\Delta t^2}{2} \frac{\partial^2 u(t)}{\partial t^2} \pm \frac{\Delta t^3}{6} \frac{\partial^3 u(t)}{\partial t^3} + \frac{\Delta t^4}{24} \frac{\partial^4 u(t)}{\partial t^4} + ...$$

We obtain $u(t + \Delta t) + u(t - \Delta t)$ to cancel the odd derivatives:

$$u(t + \Delta t) + u(t - \Delta t) = 2u(t) + \Delta t^2 \frac{\partial^2 u(t)}{\partial t^2} + \frac{\Delta t^4}{12} \frac{\partial^4 u(t)}{\partial t^4} + ...$$

Now we obtain the first derivative of $u(t \pm \Delta t)$:

$$\dot{u}(t \pm \Delta t) = \frac{\partial u(t)}{\partial t} \pm \Delta t \frac{\partial^2 u(t)}{\partial t^2} + \frac{\Delta t^2}{2} \frac{\partial^3 u(t)}{\partial t^3} \pm \frac{\Delta t^3}{6} \frac{\partial^4 u(t)}{\partial t^4} + \frac{\Delta t^4}{24} \frac{\partial^5 u(t)}{\partial t^5} + ...$$

This time we obtain $\dot{u}(t + \Delta t) - \dot{u}(t - \Delta t)$ in order to cancel the odd derivatives:

$$\dot{u}(t + \Delta t) - \dot{u}(t - \Delta t) = 2\Delta t \frac{\partial^2 u(t)}{\partial t^2} + \frac{\Delta t^3}{3} \frac{\partial^4 u(t)}{\partial t^4} + ...$$

Now we have both the wavefields and their time derivatives in terms of the second and the fourth order derivatives of the current wavefield, $u(t)$. We truncate the series after the fourth term, and apply the Lax-Wendroff scheme by replacing the second and fourth time derivatives using the two-way wave equation, thus obtaining

$$u(t + \Delta t) + u(t - \Delta t) = 2u(t) + \Delta t^2 v^2 \nabla^2 u(t) + \frac{\Delta t^4}{12} v^2 \nabla^2 [v^2 \nabla^2 u(t)]$$

and

$$\dot{u}(t + \Delta t) - \dot{u}(t - \Delta t) = 2\Delta t v^2 \nabla^2 u(t) + \frac{\Delta t^3}{3} v^2 \nabla^2 [v^2 \nabla^2 u(t)].$$

Now we can use the terms employed to compute the plain wavefields to compute the time derivatives.